J. Plasma Phys. (2021), *vol*. 87, 905870414
Published by Cambridge University Press
doi:10.1017/S0022377821000829

Radial distribution of the plasma potential in a cylindrical plasma column with a longitudinal magnetic field

G. Liziakin [1],†, A. Oiler [1,2], A. Gavrikov [1], N. Antonov [1] and V. Smirnov[1]

[1]Joint Institute for High Temperatures of the Russian Academy of Sciences (JIHT RAS), Moscow, Russia

[2]Moscow Institute of Physics and Technology (National Research University), Moscow, Russia

(Received 25 August 2020; revised 12 July 2021; accepted 21 July 2021)

The possibility of controlling the electrostatic field distribution in plasma has yielded wide prospects for modern technologies. As a magnetic field primarily allows for creating electric fields in plasma, it serves as an additional obstacle for the current flow through a medium. In the present paper, an axially symmetric system is considered in which the magnetic field is directed along the axis and concentric electrodes are located at the ends. The electrodes are negatively biased. A model which solves the problem of the radial distribution of the plasma potential inside the cylindrical plasma column supported by the end electrodes is proposed. The most commonly encountered configurations of the electrical connection for the end electrodes are considered, and the particular solutions to the problem of the radial distribution are presented. The contribution of ions and electrons to the transverse conductivity is evaluated in detail. The influence of a thermionic element on the radial profile of the plasma potential is considered. To verify the proposed model, an experimental study of the reflex discharge is carried out with both cold electrodes and a thermionic element on the axis. A comparison of the computational model results with experimental data is given. The presented model makes it possible to solve the problem concerning the plasma potential distribution in the case of an arbitrary number of end electrodes, and also to take into account the inhomogeneity of the distribution of plasma density, neutral gas pressure and electron temperature along the radius.

Key words: electric discharges, plasma applications

1. Introduction

The possibility to control the electrostatic field distribution in plasma has yielded wide prospects for modern technologies. In particular, due to the creation of a radial electric field in mirror traps, it is possible to suppress the magnetohydrodynamic instability and significantly increase the plasma confinement time (Soldatkina *et al.* 2008). In tokamaks, the appearance of a radial electric field in the H-mode has made it possible to significantly reduce transverse losses (Jain 1993; Burrell 1997), whereas the electric field realized in the Hall thrusters plasma allows for accelerating ions and thereby creates thrust (Boeuf 2017; Zolotukhin *et al.* 2020).

† Email address for correspondence: glizyakin@gmail.com

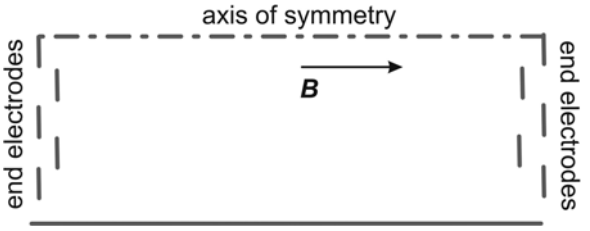

FIGURE 1. Basic diagram of a separator.

As a magnetic field primarily allows for the creation of electric fields in plasma, it serves as an additional obstacle for the current flow through the medium. At the same time, an electric field can be realized along a magnetic field if the mean free path of charged particles is substantially less than the installation size (Jin *et al.* 2019).

In the configuration of the magnetic field of a rectilinear solenoid, the creation of a radial electric field in plasma causes rotation of the entire plasma (Barber *et al.* 1972; Del Bosco *et al.* 1991). This phenomenon led to the fact that in the 1970s–1980s, various schemes of plasma centrifuges for isotope separation were proposed and actively developed (Grossman & Shepp 1991). Unlike gas centrifuges, there were no rotating parts in the plasma centrifuges, and it was assumed that the rotation speed could be higher. However, plasma centrifuges have not yet found an industrial application.

In recent decades, methods for plasma processing of spent nuclear fuel (SNF) have been actively developed (Dolgolenko & Muromkin 2017; Zweben *et al.* 2018). In SNF reprocessing (separation of fission products from actinides), a lower resolution of the device is required when compared with the separation of isotopes. Unlike plasma centrifuges, where the elements of the mixture to be separated are in collisional equilibrium, the separation in the new generation of plasma separators is supposed to be carried out in a collisionless mode.

Among the wide variety of separation schemes, there are also those in which the use of crossed electric and magnetic fields in a linear configuration is proposed (Gueroult *et al.* 2019*b*; Liziakin *et al.* 2021). The simplest scheme of such a separator is shown in figure 1. A cylindrical vacuum chamber is immersed in a longitudinal magnetic field. End electrodes are installed at the ends of the chamber. The voltages on the electrodes are provided by a power supply. At both ends, the distribution of the electrode potential is identical.

In such separators, the possibility to control the radial profile of the potential is actually the possibility to control the particle trajectories (Smirnov *et al.* 2018, 2020). Therefore, the question about the shape of the profile and the possibility of its adjustment for more efficient separation of the mixture has become particularly topical.

It is necessary to distinguish between cases when the negative potential (Liziakin *et al.* 2017) (relative to the outer cylindrical surface) and the positive one (Shinohara & Horii 2007) are maintained on the cylinder axis. The difference between these cases consists primarily of the difference between the areas of the negative and positive electrodes. An ion current flows to the negative electrode; its density is much lower than the electron one. For a stationary state, when the total charge of the system is preserved, the magnitude of the current in the system is determined by the area of the electrode collecting ions. The area of the end electrodes, as a rule, is much smaller than the area of the outer cylindrical surface. Hence the current between the electrodes, in the case of negatively biased end electrodes, will be significantly less than for the case of positively biased ones. The present study will focus on the case with negatively biased electrodes.

https://doi.org/10.1017/S0022377821000829 Published online by Cambridge University Press

Liziakin *et al.* (2020) considered the formation mechanism of a negative potential on the axis of a cylindrical plasma column immersed in a magnetic field. The formula was obtained with which it is possible to estimate the plasma column potential. The current paper will deepen the analysis of such a system and consider the shape of the potential profile.

In the present study, it will be assumed that the plasma along the magnetic field is conducting perfectly. This assumption should be clarified. In a number of cases, the longitudinal conductivity can make a significant contribution to the electric potential distribution even in a magnetized plasma. This can happen because the electrode that sets the potential has small geometrical dimensions compared with the interelectrode distance (Gilmore *et al.* 2015; Gueroult *et al.* 2016; Jin *et al.* 2019). Poulos (2019) introduced a dimensionless parameter

$$s = \frac{a}{L}\sqrt{\frac{\sigma_{||}}{\sigma_{\perp}}}, \tag{1.1}$$

where a is the radius of the electrode that sets the potential, L is the cylinder length, and $\sigma_{||}, \sigma_{\perp}$ are the longitudinal and transverse plasma conductivities, respectively. Gueroult *et al.* (2019*a*) verified that in the experiments with end electrodes in which s^{-1} was much less than one, the potential was reproduced well. On the other hand, in those experiments where this parameter was of the order of one, a significant change in the plasma potential along the column was observed. Therefore, assuming that the plasma along the magnetic field is ideally conducting, one should have in mind that this parameter is much less than one and, as a result, the change in potential along the magnetic field is negligible.

It should be noted that the ideal conductivity of the plasma in the longitudinal direction does not mean that the density of the current between the electrode and the plasma can reach arbitrarily large values. There is a thin near-electrode layer between these objects. In this layer, it is no longer possible to speak of ideal conductivity, and it is precisely that which can serve as a limiter for the longitudinal current density.

Although in many experimental papers, the end electrodes were made of a large number of concentric electrodes (>2), quite often, all electrodes were divided into one or two groups of short-circuited electrodes and the same voltage was applied to each group of electrodes (Amatucci *et al.* 1996; Shinohara & Horii 2007). Thus, a group of short-circuited electrodes effectively acted as a single electrode. In this work, we will consider both the cases of such electrode connections and the general case of independent connection of more than two electrodes.

The main objective of the work is to derive the dependence of the plasma potential radial distribution on the end electrodes potential radial distribution.

To verify the proposed model, we conducted an experimental study and compared its results with the predictions of the model.

2. Ohm's law

Let us consider an axially symmetric system in which the magnetic field is directed along the axis (see figure 1). Let concentric electrodes be placed at the ends of such a system, while the interelectrode gap is filled with plasma.

Although the transverse conductivity across the magnetic field can be influenced by a large number of parameters, which include various types of instabilities, we will consider classical conductivity. Thus, this calculation can be considered as a lower estimate.

In the hydrodynamic plasma model, one can obtain the generalized Ohm's law from the momentum balance equations. Neglecting the motion of neutrals in the laboratory coordinate system (Paschmann *et al.* 2003), one can obtain the radial component of

https://doi.org/10.1017/S0022377821000829 Published online by Cambridge University Press

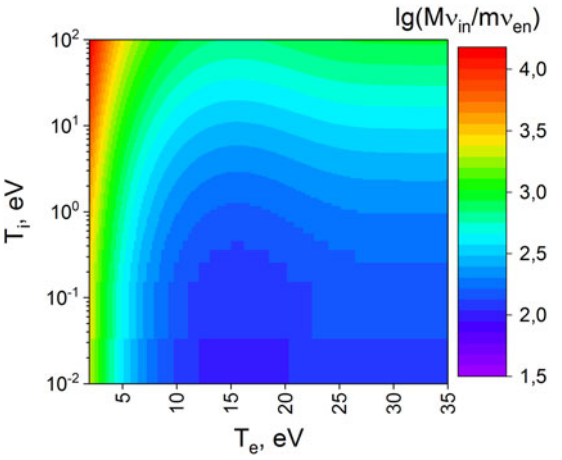

FIGURE 2. Relation between $M\nu_{in}$ and $m\nu_{en}$ in argon.

current density

$$j_r = \sigma_P^n E_r, \tag{2.1}$$

where E_r is the radial electric field and σ_P^n is the transverse conductivity in the rest frame of neutrals.

Let us show that in a certain range of parameters, the main contribution to the transverse conductivity is made by collisions of ions with neutrals. In the model of three liquids (ions, electrons and neutral atoms), the transverse conductivity in the rest system of neutrals has the form (Song *et al.* 2001)

$$\sigma_P^n = \frac{en_e}{B}\frac{\kappa}{(\kappa)^2+1}, \quad \text{where } \kappa = \frac{\Omega_i}{\nu_{in}} + \frac{\nu_{en}}{\Omega_e} + \frac{\nu_{ei}}{\Omega_e}. \tag{2.2}$$

Here, Ω_i, Ω_e are the Larmor frequencies of rotation of ions and electrons, while ν_{in}, ν_{en}, ν_{ei} are the corresponding collision frequencies. In obtaining this equation, the relation $M\nu_{in} \gg m\nu_{en}$ was assumed to be correct. As shown in figure 2, it is valid in a wide range of plasma parameters, in particular, for argon in the range of $T_e \in [2, 35]$ eV, $T_i \in [0.01, 100]$ eV. When obtaining figure 2, the values of the elastic collisions cross-section of ions with neutrals in the energy range of 4–400 eV were used from the study by Cramer (1959). At lower energies, we used (2.26) from Raizer *et al.* (2011), which determines the polarization cross-section. For the elastic collisions cross-section of electrons with neutrals we used the data from Ramsauer (1922).

As follows from (2.2) the relationship between the magnetization parameters of electrons and ions determines which of the particle species makes the largest contribution to the transverse transport. Figure 3 shows the components κ in their dependence on the magnetic field, neutral gas pressure and plasma density for argon. When analysing this graph, it should be considered that the upper and lower horizontal axes can be changed independently, since they are defined by different components of κ. So the lower axis determines the components Ω_i/ν_{in} and ν_{en}/Ω_e, and the upper one ν_{ei}/Ω_e.

To the right of the dashed line in figure 3, there is a domain where the ionic conductivity is more than 10 times greater than the electronic one. Most experiments with end electrodes are performed using the parameters from this domain (Gueroult *et al.* 2019*a*; Liziakin *et al.* 2020). Therefore, it will be further assumed that the plasma conductivity

https://doi.org/10.1017/S0022377821000829 Published online by Cambridge University Press

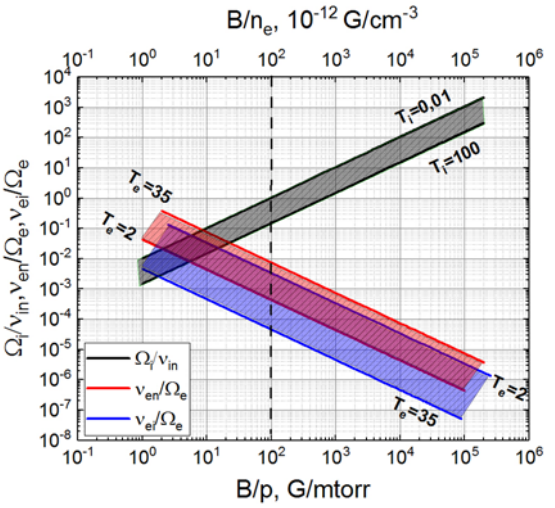

FIGURE 3. Comparison of the contribution of electrons and ions to the transverse conductivity of plasma. The dashed line indicates the excess of ionic conductivity over the electronic one by 10 times in the considered temperature range of electrons and ions.

across the magnetic field is determined by the transport of ions. However, it is worth remembering that such a consideration is true only for the indicated B/p and B/n_e. In this case, the conductivity takes the form

$$\sigma_P^n = \frac{en_e}{B}\frac{\chi}{(\chi)^2+1} = \frac{e^2 n_e}{M\nu_{in}}\frac{1}{(\chi)^2+1}, \quad \text{where } \chi = \frac{\Omega_i}{\nu_{in}} = \frac{eB}{M}\frac{1}{n_n\sigma_{in}u_i}. \tag{2.3}$$

Here σ_{in} is the elastic collisions cross-section of ions with neutrals.

3. Radial profile of the potential

It was found in the previous section that in the considered parameter range, the main current across the magnetic field was transported by ions.

Consider the relation between the plasma potential and the potential of the end electrodes in the case when the potential of electrodes monotonically increases with r ($U_{e1} < U_{e2}$). Figure 4 shows an equivalent electrical circuit. The outer cylindrical surface and electrode 3 are grounded, and their potentials are equal to zero ($U_{e3} = 0$). On the two inner electrodes (U_{e1}, U_{e2}), a negative potential relative to electrode 3 is maintained by the external power source. The symbols V_{sh1}, V_{sh2} indicate the near-electrode potential drop. We should point out that the discrete current loops schematically indicated in figure 4 are in fact continuous, and the magnitude of the near-electrode potential drop is radially varying.

The elementary increment of the plasma potential along the radius can be written in the form

$$\mathrm{d}U(r) = I_r(r)\,\mathrm{d}R(r), \tag{3.1}$$

where

$$\mathrm{d}R(r) = \frac{1}{\sigma_P^n(r)}\frac{\mathrm{d}r}{2\pi rL}, \tag{3.2}$$

whereas I_r is the total current along the radial coordinate and L is the length of the plasma cylinder. Taking into account the stationarity of the flow of currents and the law of the

https://doi.org/10.1017/S0022377821000829 Published online by Cambridge University Press

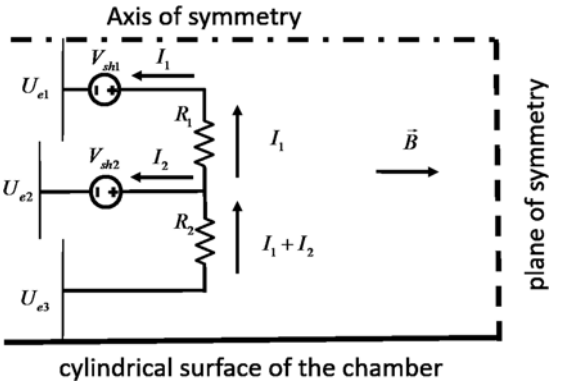

FIGURE 4. Equivalent electrical circuit of an axisymmetric system with an axial magnetic field and end electrodes.

charge conservation, one can find that the radial current in an arbitrary coordinate r should be equal to the total current of all the electrodes located in the region $\tilde{r} < r$

$$I_r(r) = \int_0^r j(\tilde{r})\,\mathrm{d}S(\tilde{r}), \tag{3.3}$$

where j is the density of current to the end electrodes and $\mathrm{d}S = 2\pi\tilde{r}\,\mathrm{d}\tilde{r}$. Therefore, the plasma potential at an arbitrary point should be equal to

$$U(r) = \int_{r_g}^r \int_0^{\hat{r}} j(\tilde{r})\,\mathrm{d}S(\tilde{r})\frac{1}{\sigma_P^n(\hat{r})}\frac{\mathrm{d}\hat{r}}{2\pi\hat{r}L}, \tag{3.4}$$

where $\tilde{r}$, $\hat{r}$ are integration variables and r_g is the inner edge of the grounded electrode.

The plasma conductivity under the integral is a function of the ion velocity, which in turn is a function of the radial electric field.

3.1. *Strongly negative equipotential end*

The simplest case of connecting the end electrodes is by short-circuiting all of the electrodes to each other except for the outermost one ($U_{e1} = U_{e2}$, while $U_{e3} = 0$, figure 4). A large negative potential $eU_e \gg T_e$ is applied to electrodes 1 and 2. This configuration looks most like a classical reflex discharge (Liziakin *et al.* 2016). In this case, j from (3.4) can be substituted by the density of the ion saturation current (Lieberman & Lichtenberg 2005) $j_{is} = 0.52en(kT_e)^{0.5}M^{-0.5}$ times the number of ends with electrodes N_{surf} (1 or 2). If one assumes that the neutral density, plasma density, electron temperature and the cross-section of elastic collisions of ions with neutrals do not depend on the radial coordinate, then the potential increment along the radius can be represented in the form

$$-\mathrm{d}U(r) = \frac{0.52}{e}\frac{M^{0.5}(kT_e)^{0.5}n_n\sigma_{in}N_{\mathrm{surf}}}{BL}\int_0^{\hat{r}}(\tilde{r}\,\mathrm{d}\tilde{r})\left(U'(\hat{r})\left[1+\left(\frac{eB^2}{Mn_n\sigma_{in}}\frac{1}{U'(\hat{r})}\right)^2\right]\right)\frac{\mathrm{d}\hat{r}}{\hat{r}}. \tag{3.5}$$

Here, for simplification, σ_{in} is taken to be constant and is equal to 2.5×10^{-15} cm^2, whereas the velocity of ions equals $u_i = E/B = U'/B$. Then, performing integration with

https://doi.org/10.1017/S0022377821000829 Published online by Cambridge University Press

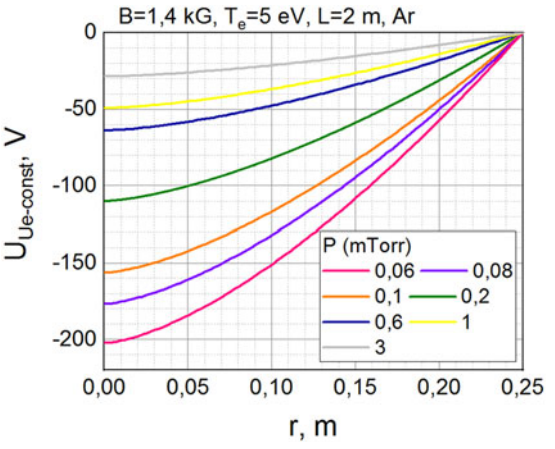

FIGURE 5. Potential radial profile in the configuration when all the electrodes (except for the external grounded electrode) are at a large negative potential $eU_e \gg T_e$.

respect to the variable $\tilde{r}$ and denoting

$$C_1 = \frac{0.52}{2e}\frac{M^{0.5}(kT_e)^{0.5}n_n\sigma_{in}N_{\text{surf}}}{BL}, \quad C_2 = \left(\frac{eB^2}{Mn_n\sigma_{in}}\right)^2, \tag{3.6a,b}$$

one can get

$$U(r) = C_1\int_{r_g}^{r}\hat{r}U'(\hat{r})\left(1+\frac{C_2}{(U'(\hat{r}))^2}\right)\mathrm{d}\hat{r} + U(r_g). \tag{3.7}$$

Differentiating both sides of (3.7), expressing U' and integrating from the inner edge of the grounded electrode r_g, one can obtain

$$\begin{aligned} U(r) &= \sqrt{C_2}\int_{r_g}^{r}\sqrt{\frac{\hat{r}}{1/C_1-\hat{r}}}\,\mathrm{d}\hat{r} \\ &= \sqrt{\frac{C_2C_1r}{1-C_1r}}\frac{(\sqrt{C_1r}(C_1r-1)+\sqrt{1-C_1r}\sin^{-1}(\sqrt{C_1r}))}{C_1^{3/2}\sqrt{r}} - F(r_g) + U(r_g). \end{aligned} \tag{3.8}$$

Here and after, $F(r)$ is an antiderivative of the function. For $C_1r \ll 1$, one can expand this in a Taylor series to the first non-zero term

$$U(r) = \tfrac{2}{3}\sqrt{C_1C_2}(r^{3/2} - r_g^{3/2}) + U(r_g). \tag{3.9}$$

Figure 5 demonstrates potential profiles, calculated by (3.9) with $U(r_g) = 0$, under fixed magnetic field, electron temperature, length and radius of installation in argon gas. In this example, $r_g = 0.25$ m. The ion-saturation current is the maximal current which can flow through a layer (sheath) of a cold negative electrode. Therefore, the presented profiles are an estimate from above for the possible potential values. For the conditions shown in figure 5, the dimensionless parameter s^{-1} is in the range (2–55) $\times$ 10^{-3}.

https://doi.org/10.1017/S0022377821000829 Published online by Cambridge University Press

3.2. *Floating-gap configuration*

In the experimental implementation of the electrode geometry described in the previous section, an arc discharge may occur between negative and grounded electrodes across the magnetic field. To avoid this, one can install another electrode between these electrodes with an intermediate voltage or under a floating potential ($I_2 = 0$ in figure 4). Thus, a buffer zone appears that prevents disruption of the discharge. In this case, the plasma potential will be determined by the system of equations

$$U(r) = \begin{cases} \frac{2}{3}\sqrt{C_1 C_2}(r^{3/2} - r_e^{3/2}) + U(r_e), r \in [0, r_e] \\ \int_0^{r_e} j_{is}\,\mathrm{d}S \int_{r_g}^{r} \mathrm{d}R, \qquad\qquad r \in [r_e, r_g] \end{cases}, \tag{3.10}$$

where r_e is the outer radius of the negative electrode. Substituting j_{is} into the second equation of system (3.10) and taking into account (3.2), one can get

$$U(r) = r_e^2 C_1 \int_{r_g}^{r} U'(\hat{r}) \left(1 + \frac{C_2}{U'^2(\hat{r})}\right) \frac{\mathrm{d}\hat{r}}{\hat{r}} + U(r_g). \tag{3.11}$$

Then, similar to (3.7), differentiating both sides of (3.11), expressing U' and performing integration, one can get

$$U(r) = 2\sqrt{r_e^2 C_1 C_2}\left(\sqrt{r - r_e^2 C_1} - \sqrt{r_g - r_e^2 C_1}\right) + U(r_g), \quad r \in [r_e, r_g]. \tag{3.12}$$

3.3. *Thermionic element on the axis of the system*

Equation (3.1) shows that an increase in the potential of the plasma volume can be achieved by increasing the radial current. In an experimental implementation, this can be done by using a thermionic cathode.

When electrons are injected into a vacuum, their current is limited by the Child–Langmuir law (Langmuir & Compton 1931). When electrons are injected into neutral plasma, the space charge of electrons is compensated by the space charge of ions in the cathode layer. Although the current of thermoelectrons can significantly exceed the ion-saturation current, its magnitude is bounded just the same. At a low-ion-saturation current, a virtual cathode is formed. The critical thermionic current as a function of the potential of the cathode layer was found by Poulos (2019).

Consider the case when a thermal cathode with a radius r_{th} is situated on the axis. Then the potential increment along the radius will be a piecewise-defined function

$$\mathrm{d}U = \begin{cases} \left(\int_0^{r} j_{\text{th}}(\tilde{r})\,\mathrm{d}S + \int_0^{r} j_{is}(\tilde{r})\,\mathrm{d}S\right) \mathrm{d}R, r \in [0, r_{\text{th}}] \\ \left(\int_0^{r_{\text{th}}} j_{\text{th}}\,\mathrm{d}S + \int_0^{r} j_{is}(\tilde{r})\,\mathrm{d}S\right) \mathrm{d}R, \quad r \in [r_{\text{th}}, r_e] \\ \left(\int_0^{r_{\text{th}}} j_{\text{th}}\,\mathrm{d}S + \int_0^{r_e} j_{is}\,\mathrm{d}S\right) \mathrm{d}R, \qquad r \in [r_e, r_g] \end{cases}. \tag{3.13}$$

Denoting

$$C_3 = \frac{M n_n \sigma_{in} N_{\text{surf}}}{2e^2 n_e B L}, \tag{3.14}$$

https://doi.org/10.1017/S0022377821000829 Published online by Cambridge University Press

and considering that

$$C_1 = j_{is} C_3, \tag{3.15}$$

one can obtain, similar to the previous sections,

$$U(r) = \begin{cases} \frac{2}{3}\sqrt{(j_{\text{th}} + j_{is})C_3 C_2}(r^{3/2} - r_{\text{th}}^{3/2}) + U(r_{\text{th}}), & r \in [0, r_{\text{th}}] \\ \displaystyle\int_{r_e}^{r} \sqrt{\frac{(j_{\text{th}} r_{\text{th}}^2 + j_{is} r^2)C_3 C_2}{r - (j_{\text{th}} r_{\text{th}}^2 - j_{is} r^2)C_3}}\, \mathrm{d}r + U(r_e), & r \in [r_{\text{th}}, r_e] \\ 2\sqrt{(j_{\text{th}} r_{\text{th}}^2 + j_{is} r_e^2)C_3 C_2}\sqrt{r - (j_{\text{th}} r_{\text{th}}^2 + j_{is} r_e^2)C_3} - F(r_g) + U(r_g), & r \in [r_e, r_g] \end{cases}. \tag{3.16}$$

The constants in the expression are chosen so the function is continuous.

3.4. *Slightly negative electrodes*

In §§3.1–3.3, particular cases of connecting end electrodes to an electrical circuit were considered. The main simplification that allowed obtaining analytical equations for $U(r)$ is that a large negative potential $eU_e \gg T_e$ is applied to the negative electrode. In these cases, as seen from (3.9), (3.12) and (3.16), the plasma potential does not depend on the electrode potential. For such a voltage, the electrons from the plasma cannot get onto the negative electrode, and therefore their current can be neglected. In this section, we consider the case when the electrodes are slightly negative biased ($eU_e \sim T_e$). In this case I_r from (3.1) should be written in the form

$$I_r(r) = 2\pi \int_0^r \left(j_{es}(\tilde{r}) exp\left(\frac{e(U_e(\tilde{r}) - U(\tilde{r}))}{kT_e} \right) - j_{is}(\tilde{r}) \right) \tilde{r}\, \mathrm{d}\tilde{r}. \tag{3.17}$$

Since now the potential of the electrode may not differ much from the potential of the plasma ($eU_e/T_e \sim 1$), regions may appear where $U'(r) \to 0$, in this case, in (2.3) for the collision frequency, the ion thermal velocity u_T should be added

$$u_i = \frac{U'(\hat{r})}{B} + u_T. \tag{3.18}$$

For u_T we use room temperature of 300 K.

If the discharge is self-sustained, that is, the plasma is created only by electrodes, then the area occupied by the plasma is bounded by the condition $r < r_g$. If the plasma is maintained by an external ionization source (electron beam (Maggs *et al.* 2007), radio-frequency (rf) discharge (Litvak *et al.* 2003; Shinohara & Horii 2007; Gilmore *et al.* 2015; Gueroult *et al.* 2016; Liziakin *et al.* 2017; Vorona *et al.* 2019), microwave plasma source (Amatucci *et al.* 1996)), then the plasma density may not be equal to zero for $r > r_g$. In this case, when moving away along the radius from the inner edge of the grounded electrode, the plasma potential tends to the value

$$U(r > r_g) = T_e \ln\left(\sqrt{\frac{\pi}{2}\frac{m}{M}} \right). \tag{3.19}$$

https://doi.org/10.1017/S0022377821000829 Published online by Cambridge University Press

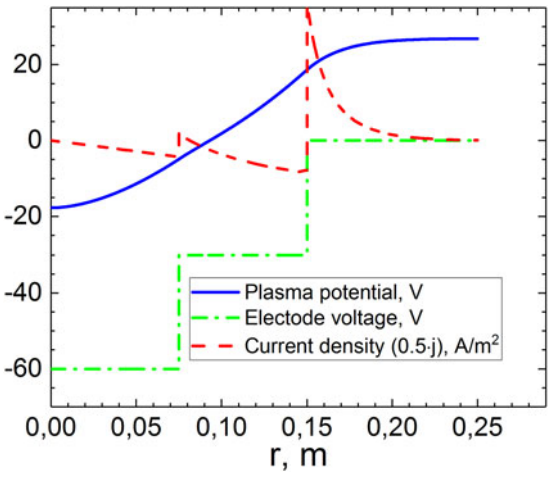

FIGURE 6. An example of solving (3.20) with parameters $B = 1.4$ kG, $P = 0.2$ m Torr, $n_e = 10^{11}$ cm^{-3}, $T_e = 5$ eV.

Then the distribution of the plasma potential is the solution of the equation

$$U(r) = \frac{Mn_n}{e^2 L}\int_{r_{ex}}^{r}\int_{0}^{\hat{r}}\left(j_{es}(\tilde{r})exp\left(\frac{e(U_e(\tilde{r}) - U(\tilde{r}))}{kT_e}\right) - j_{is}(\tilde{r})\right)\tilde{r}\,\mathrm{d}\tilde{r}\sigma_{in}$$
$$\times\left(1 + \left(\frac{eB}{Mn_a\sigma_{in}}\right)^2 \frac{1}{\left(\frac{U'(\hat{r})}{B} + v_T\right)^2}\right)$$
$$\times\left(\frac{U'(\hat{r})}{B} + v_T\right)\frac{1}{n(\hat{r})}\frac{\mathrm{d}\hat{r}}{\hat{r}} + U(r_{ex}). \tag{3.20}$$

Here, integration is carried out from the outer boundary r_{ex} of the electrode system. It is also considered in this equation that the plasma density and electron temperature depend on the radial coordinate. A methodology for numerically solving this equation is presented in Appendix A. The computer program LaPotential that solves this equation is presented by Oiler & Liziakin (2021).

An example of the calculation results for a case when the voltage at the electrodes is not large ($eU_e/T_e \sim 1$) is presented in figure 6. A positive current density corresponds to the electronic current to the electrodes, whereas a negative value corresponds to the ionic current.

4. Comparison with experimental data

To test the model described above, a series of experiments was carried out. The experimental set-up is shown in figure 7. The vacuum chamber was a cylinder with a diameter of 85 cm and a length of 220 cm. A longitudinal magnetic field was created by a four-coil solenoid. On the chamber axis, the magnetic field was 1.4 kG. The working gas was argon at a pressure of 0.3 mTorr.

End electrodes in the form of truncated cones were placed at the ends of the chamber. Three internal electrodes ($r < 15$ cm) from each end were connected between one another

https://doi.org/10.1017/S0022377821000829 Published online by Cambridge University Press

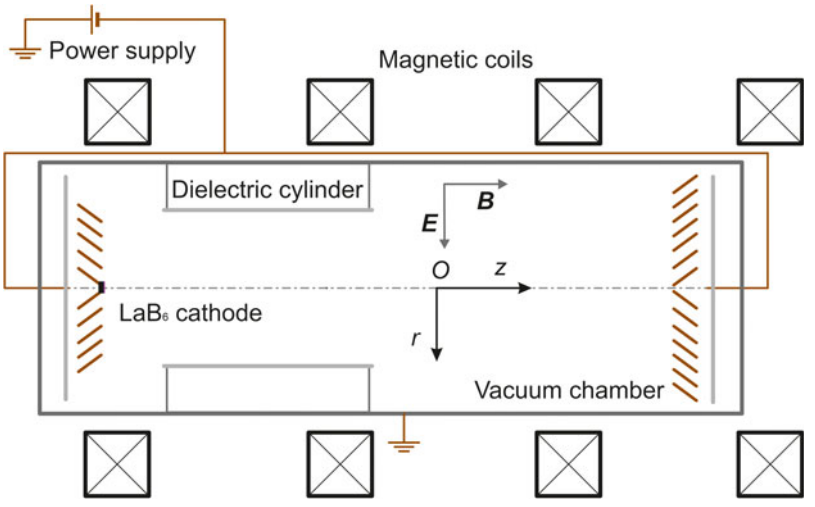

FIGURE 7. Experimental scheme.

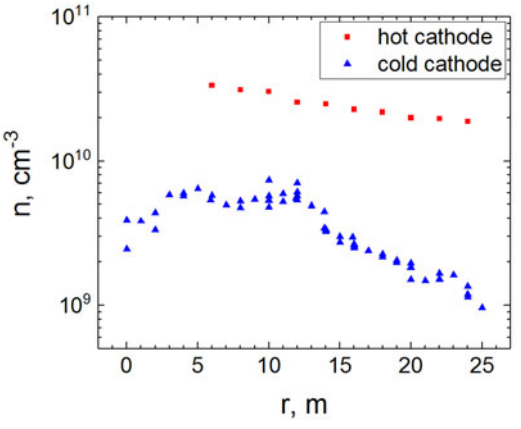

FIGURE 8. Radial profile of the plasma density.

and constant voltage was maintained on them. The fourth and fifth electrodes ($15 < r < 25$ cm) were under floating potential. The walls with $r > 25$ cm were at ground potential. A thermal cathode made of LaB_6 with a diameter of 2 cm was installed at the left end (figure 7) in the very centre of the electrode. The emissive electrode was electrically connected with three internal electrodes. The end electrodes, together with the grounded cylindrical surface of the vacuum chamber, formed the geometry of the reflex discharge (Hooper 1970). Two modes of discharge functioning were investigated. The first mode was when the thermal cathode is not heated, that is, the discharge operates as a usual reflex discharge with cold electrodes. The second mode was when the thermal cathode is heated. In the first case, the voltage at the electrodes was maintained at a level of -1 kV, while the discharge current was 50 mA; in the second case, the voltage was -0.5 kV, and the current was 10 A. The density profiles in both modes are presented in figure 8. Table 1 summarizes the parameters of both modes. The calculated values for s^{-1} correspond to 0.01 and 0.03 for the cold and hot modes, respectively.

https://doi.org/10.1017/S0022377821000829 Published online by Cambridge University Press

Mode	Discharge voltage (V)	Discharge current (A)	Averaged plasma density (cm^{-3})	Gas pressure (mTorr)	Electron temperature (eV)
Cold cathode	1000	0.05	3.7×10^9	0.3	2–4
Hot cathode	500	10	2.5×10^{10}	0.5	8.5

TABLE 1. Experimental parameters of the reflex discharge.

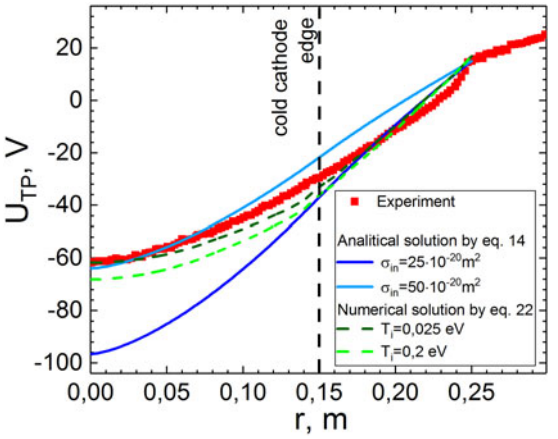

FIGURE 9. Comparison of the plasma potential profile calculated by the system of (3.10) with the experimental one without a thermal cathode.

Plasma density and electron temperature were measured by the double probe, and the plasma potential was measured with an emission probe (Murzaev *et al.* 2019). The temperature of electrons weakly depended on the radial coordinate and was 4 eV in the electrode region and 2 eV in the floating electrode region for the cold cathode mode. For the hot cathode mode, the electron temperature was $T_e = 8.5 \pm 1.5$ eV.

Figure 9 presents a comparison of the plasma potential profile calculated by the system of (3.10) and that obtained experimentally in the mode with cold electrodes. Two profiles are presented with different cross-sections. The first profile corresponds to elastic collisions $\sigma_{in} = 25 \times 10^{-20}$ m^2 and the second corresponds to the sum of elastic and charge exchange cross-section $\sigma_{in} = 50 \times 10^{-20}$ m^2. Thus, there is an input parameter in this model that could quantitatively affect predictions, and these parameters are not all well-constrained experimentally. While $U \sim \sigma_{in}^{-0.5} T_e^{0.25}$ doubling the cross-section gives the same result as decreasing T_e by 4 times. It can be reasonable to consider that the double probe method can overestimate T_e. Figure 9 also shows the numerical solution of (3.20) by LaPotential taking into account polarization cross-section, space variation of plasma density and electron temperature, and ion temperatures with T_i equal to 0.025 and 0.2 eV. Taking these features into account significantly improved the agreement with the experimental data. Figure 10 shows a comparison of the plasma potential profile calculated using the system of (3.16) with the experimental one under the operation of the thermal cathode with a current of 5.6 A. To exclude the influence of anode processes (not considered in this article), we set the calculated values of the plasma potential at $r_g = 25$ cm, equal to the experimental value at this point. In both cases, good agreement

https://doi.org/10.1017/S0022377821000829 Published online by Cambridge University Press

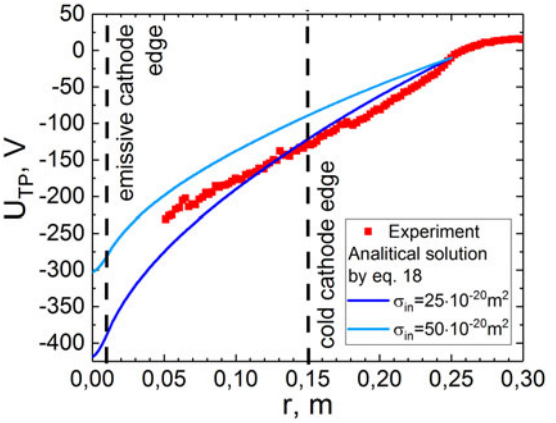

FIGURE 10. Comparison of the plasma potential profile calculated by the system of (3.16) with the experimental one under the thermal cathode functioning with a current of 5.6 A.

Mode	M (u)	T_e (eV)	n_n (cm^{-3})	σ_{in} (10^{-20} m^2)	N_{surf}	B (kG)	L (m)	n_i (cm^{-3})	I_{th} (A)
Cold cathode	40	4	9.7×10^{12}	25…50	2	1.4	2	—	—
Hot cathode	40	8.5	1.6×10^{13}	25…50	2	1.4	2	2.5×10^{10}	5.6

TABLE 2. Input parameters of theoretical model for analytical solution.

was observed between the experimental and theoretical values. All parameters that are used in the theoretical model are summarized in table 2.

5. Discussion

Consider some specific features of the formation of the radial plasma potential following from (3.9), (3.12) and (3.16). From (3.5) it follows that, in the approximation of constant plasma density, the potential profile does not depend on the plasma density. This statement is true for a configuration with a strongly negative equipotential end ($eU_e \gg T_e$). Therefore, if the task is simply to obtain a potential difference in the radial direction, then it makes no sense to transfer much energy into the plasma to increase its density. Besides, the plasma potential is proportional to the ion mass raised to the power of -0.75. This means that with the same parameters as presented in figure 5, but with a lighter gas, for example, with helium, a voltage drop 5.6 times greater than that with argon can be obtained.

From (3.12) it follows that the use of a floating intermediate electrode leads to a decrease in the radial electric field. While under a strongly negative electrode, the potential grew as $r^{3/2}$ in its dependence on the radius, under a floating electrode it grows only as $r^{1/2}$. When using a thermionic cathode, in accordance with (3.16), a dependence of the potential on the plasma density appears. A larger plasma density will result in a smaller potential drop at the same emission current. It must be kept in mind that the plasma density inside the thermal cathode domain $r < r_{\text{th}}$ can be very different from that at the external region.

Equation (3.20) is written without assuming the uniformity of the spatial distribution of the plasma density. This is important because the density cannot always be considered to be constant. It can decrease by 2 orders of magnitude over several centimetres (Liziakin *et al.* 2017), and replacing such a profile with a uniform one can significantly distort the

https://doi.org/10.1017/S0022377821000829 Published online by Cambridge University Press

real picture. The good agreement between the calculated profiles and the experiment in the current study is largely due to the fact that the density profile in the experiment was quite flat.

6. Conclusion

The paper considers the problem of creating a radial electric field in a cylindrical plasma column. The case of negative biases is considered. The analytical solutions for the radial potential profile of three most useful electrode configurations are found, by assuming that ion velocity is determined by the E/B relation, and neutral density, plasma density, electron temperature and the elastic collisions cross-section are all constant. In a configuration with a strongly negative equipotential end ($eU_e \gg T_e$), it is shown that the plasma potential grows as $r^{3/2}$. When a floating electrode is added between the negative and the ground electrodes, the plasma potential grows only as $r^{1/2}$. The mechanism of how the thermionic current at the end allows an increase in the radial potential drop is also shown. An equation is derived for the case when the end electrodes are under potentials close to the plasma potential. The solver LaPotential for the equation is presented which can consider the spatial non-uniformity of electron density and temperature, and the cross-section dependence on ion velocity. To verify the proposed model, an experimental study of the reflex discharge with cold electrodes and with a thermionic cathode was carried out. A comparison of the results of the calculation model with experimental data showed their good agreement.

Declaration of interests

The authors report no conflict of interest.

Funding

This work was partially supported by the Ministry of Science and Higher Education of the Russian Federation (G.L., A.O., MK-2403.2020.2), (State Assignment No. 075-00460-21-00).

Editor Troy Carter thanks the referees for their advice in evaluating this article.

Data availability statement

The data that support the findings of this study are available from the corresponding author upon reasonable request.

Appendix A

Equation (3.20) presented in § 3.4 of this paper can be rewritten as

$$U(r) = U(r_{ex}) - \int_{r_{ex}}^{r} \int_{0}^{\hat{r}} \left(A_1 exp\left(\frac{U_e(\tilde{r}) - U(\tilde{r})}{A_3} \right) - A_2 \right) n(\tilde{r}) \tilde{r}\, \mathrm{d}\tilde{r} \times \left(U'(\hat{r}) + A_5 + \frac{A_4}{U'(\hat{r}) + A_5} \right) \frac{1}{n(\hat{r})} \frac{\mathrm{d}\hat{r}}{\hat{r}}, \tag{A1}$$

here $A_2 = 0.52(n_n \sigma_{in}/LBe) N_{\mathrm{surf}} \sqrt{MkT_e}$; $A_1 = A_2 \sqrt{2M/\pi m}$; $A_3 = T_e$; $A_4 = e^2 B^4 / (M n_n \sigma_{in})^2$; $A_5 = B v_T = B\sqrt{2kT_0/M}$, T_0 is thermal ion energy.

https://doi.org/10.1017/S0022377821000829 Published online by Cambridge University Press

We consider the cross-section as

$$\sigma_{in} = \sigma_\infty + \frac{2\pi e\sqrt{\alpha}}{\sqrt{\frac{M}{2}}\frac{U'(r)}{B} + \sqrt{kT_0}}, \tag{A2}$$

where σ_∞ is cross-section on the infinity of energies, α is relative polarizability (Raizer *et al.* 2011).

According to (3.19) in § 3.4, $U(r_{ex}) = U_e(r_{ex}) - A_3 \ln(A_2/A_1)$. Let us denote

$$\eta(r) = \frac{1}{n(r)r}\int_0^r \left(A_1 exp\left(\frac{U_e(\tilde{r}) - U(\tilde{r})}{A_3}\right) - A_2\right) n(\tilde{r})\tilde{r}\,\mathrm{d}\tilde{r}. \tag{A3}$$

After differentiating (A1) with respect to r, we obtain

$$U'(r) = -\eta(r)\left(U'(r) + C_5 + \frac{C_4}{U'(r) + C_5}\right). \tag{A4}$$

Excluding $U'(r)$ from the (A4) leads to

$$U'(r) = \frac{1}{2(1+\eta(r))}(-C_5(1+2\eta(r)) \pm \sqrt{{C_5}^2 - 4C_4\eta(r)(1+\eta(r))}). \tag{A5}$$

It is not difficult to show that $\lim_{r\to 0}\eta(r) = 0$. So, from (A3) it follows that $U'(0) = 0$, consequently in (A5) $U'(0)$ has to take a + sign. Then

$$U'(r) = \frac{C_5}{2(1+\eta(r))}\left(-1 - 2\eta(r) + \sqrt{1 - \frac{4C_4\eta(r)}{{C_5}^2}(1+\eta(r))}\right). \tag{A6}$$

This equation must be solved considering the following boundary conditions:

$$U'(0) = 0, \tag{A7}$$

$$U(r_{ex}) = U_e(r_{ex}) - C_3 \ln\left(\frac{C_2}{C_1}\right). \tag{A8}$$

Equation (A6) in conjunction with the boundary conditions (A7)–(A8) solves numerically.

The program LaPotential (Oiler & Liziakin 2021) equation solves by using the shooting method. First, (A6) needs to be solved with boundary conditions (A7). After that we get an assemblage of curves $U(r)$ by varying the values of $U(0)$. From this assemblage only one function needs to be chosen which satisfies boundary condition (A8). The search for the desired function is realized by the bisection method.

To solve the Cauchy problem ((A6) with boundary initial condition (A7)), the implicit Euler scheme is used (Dahlquist & Björck 2008):

$$\frac{U_{N+1} - U_N}{h} = \frac{C_5}{2(1+\eta(r_{N+1}))}\left(1 + \sqrt{1 - \frac{4C_4\eta(r_{N+1})}{{C_5}^2}(1+\eta(r_{N+1}))}\right) - C_5, \tag{A9}$$

where h is an integration step, and

$$\eta(r_{N+1}) = \frac{1}{((N+1)h)n((N+1)h)}\sum_{k=0}^{N+1} h\left(C_1 exp\left(\frac{U_e(kh) - U_k}{C_3}\right) - C_2\right) n(kh)kh. \tag{A10}$$

https://doi.org/10.1017/S0022377821000829 Published online by Cambridge University Press

If in the system in question there is a floating electrode, where the current density is equal to 0, then the corresponding member of the sum is equal to 0. Value U_{N+1} on the next integration step finds as a solution of nonlinear (A9) by means of the Newton method.

REFERENCES

Amatucci, W.E., Walker, D.N., Ganguli, G., Antoniades, J.A., Duncan , D., Bowles, J.H., Gavrishchaka, V. & Koepke, M.E. 1996 Plasma response to strongly sheared flow. *Phys. Rev. Lett*. **77** (10), 1978.

Barber, P.B., Swift, D.A. & Tozer, B.A. 1972 The formation of rotating plasmas in a homopolar configuration. *J. Phys.* D*: Appl. Phys.* **5** (4), 693.

Boeuf, J.-P. 2017 Tutorial: physics and modeling of Hall thrusters. *J. Appl. Phys*. **121** (1), 11101.

Burrell, K.H. 1997 Effects of E$\times$$ B velocity shear and magnetic shear on turbulence and transport in magnetic confinement devices. *Phys. Plasmas* **4** (5), 1499–1518.

Cramer, W.H. 1959 Elastic and inelastic scattering of low-velocity ions: Ne+ in A, A+ in Ne, and A+ in A. *J. Chem. Phys*. **30** (3), 641–642.

Dahlquist, G. & Björck, Å 2008 *Numerical Methods in Scientific Computing*, vol. I. SIAM.

Del Bosco, E., Simpson, S.W., Dallaqua, R.S. & Montes, A. 1991 Speed of rotation in a vacuum arc centrifuge. *J. Phys.* D*: Appl. Phys.* **24** (11), 2008.

Dolgolenko, D.A. & Muromkin, Y.A. 2017 Separation of mixtures of chemical elements in plasma. *Phys. Uspekhi* **60** (10), 994.

Gilmore, M., Lynn, A.G., Desjardins, T.R., Zhang, Y., Watts, C., Hsu, S.C., Betts, S., Kelly, R. & Schamiloglu, E. 2015 The HelCat basic plasma science device. *J. Plasma Phys*. **81** (1).

Grossman, M.W. & Shepp, T.A. 1991 Plasma isotope separation methods. *IEEE Trans. Plasma Sci*. **19** (6), 1114–1122.

Gueroult, R., Evans, E.S., Zweben, S.J., Fisch, N.J. & Levinton, F. 2016 Initial experimental test of a helicon plasma based mass filter. *Plasma Sources Sci. Technol*. **25** (3), 35024.

Gueroult, R., Rax, J.-M. & Fisch, N.J. 2019*a* A necessary condition for perpendicular electric field control in magnetized plasmas. *Phys. Plasmas* **26** (12), 122106.

Gueroult, R., Zweben, S.J., Fisch, N.J. & Rax, J.-M. 2019*b* ExB configurations for high-throughput plasma mass separation: an outlook on possibilities and challenges. *Phys. Plasmas* **26** (4), 43511.

Hooper, E.B. Jr. 1970 A review of reflex and penning discharges. In *Advances in Electronics and Electron Physics* (ed. L. Marton & M. Claire), vol. 27, pp. 295–343. Academic Press.

Jain, K.K. 1993 Observation of improved behavior by electrode biasing of a toroidal plasma having no poloidal magnetic field. *Phys. Rev. Lett*. **70** (6), 806–809.

Jin, S., Poulos, M.J., Van Compernolle, B. & Morales, G.J. 2019 Plasma flows generated by an annular thermionic cathode in a large magnetized plasma. *Phys. Plasmas* **26** (2), 22105.

Langmuir, I. & Compton, K.T. 1931 Electrical discharges in gases part II. Fundamental phenomena in electrical discharges. *Rev. Mod. Phys*. **3** (2), 191–257.

Lieberman, M.A. & Lichtenberg, A.J. 2005 *Principles of Plasma Discharges and Materials Processing*. John Wiley & Sons.

Litvak, A., Agnew, S., Anderegg, F., Cluggish, B., Freeman, R., Gilleland, J., Isler, R., Lee, W., Miller, R., Ohkawa, T., Putvinski, S., Sevier, L., Umstadter, K. & Winslow, D. 2003 Archimedes plasma mass filter. In *30th EPS Conference on Controlled Fusion and Plasma Physics*, St. Petersburg. 7-11 July vol. 27, O-1.6 A.

Liziakin, G., Antonov, N., Usmanov, R., Melnikov, A., Timirkhanov, R., Vorona, N., Smirnov, V.S., Oiler, A., Kislenko, S., Gavrikov, A. & Smirnov, V.P. 2021 Experimental demonstration of plasma mass separation in a configuration with a potential well and crossed electric and magnetic fields. *Plasma Phys. Control. Fusion* **63** (3), 032002.

Liziakin, G.D., Gavrikov, A.V., Murzaev, Y.A., Usmanov, R.A. & Smirnov, V.P. 2016 Parameters influencing plasma column potential in a reflex discharge. *Phys. Plasmas* **23** (12), 123502.

https://doi.org/10.1017/S0022377821000829 Published online by Cambridge University Press

LIZIAKIN, G., GAVRIKOV, A. & SMIRNOV, V. 2020 Negative electric potential in a cylindrical plasma column with magnetized electrons. *Plasma Sources Sci. Technol*. **29** (1), 15008.

LIZIAKIN, G., GAVRIKOV, A., USMANOV, R., TIMIRKHANOV, R. & SMIRNOV, V. 2017 Electric potential profile created by end electrodes in a magnetized rf discharge plasma. *AIP Adv*. **7** (12).

MAGGS, J.E., CARTER, T.A. & TAYLOR, R.J. 2007 Transition from Bohm to classical diffusion due to edge rotation of a cylindrical plasma. *Phys. Plasmas* **14** (5), 52507.

MURZAEV, Y., LIZIAKIN, G., GAVRIKOV, A., TIMIRKHANOV, R. & SMIRNOV, V. 2019 A comparison of emissive and cold floating probe techniques for electric potential measurements in rf inductive discharge. *Plasma Sci. Technol*. **21** (4), 45401.

OILER, A. & LIZIAKIN, G. 2021 *Program LaPotential*. Available at: http://laplas.su/resources/.

PASCHMANN, G., HAALAND, S. & RUDOLF, T. 2003 *Auroral Plasma Physics*. Springer.

POULOS, M.J. 2019 Model for the operation of an emissive cathode in a large magnetized-plasma. *Phys. Plasmas* **26** (2), 22104.

RAIZER, Y.P., KISIN, V.I. & ALLEN, J.E. 2011 *Gas Discharge Physics*. Springer. Available at: http://books.google.ru/books?id{\mathsurround=\opskip$=$}zd-KMAEACAAJ.

RAMSAUER, C. 1922 Über den Wirkungsquerschnitt der Gasmoleküle gegenüber langsamen Elektronen. I. Fortsetzung. *Ann. Phys*. **371** (24), 546–558.

SHINOHARA, S. & HORII, S. 2007 Initial trial of plasma mass separation by crossed electric and magnetic fields. *Japan. J. Appl. Phys*. **46** (7R), 4276.

SMIRNOV, V.P., GAVRIKOV, A.V., SIDOROV, V.S., TARAKANOV, V.P., TIMIRKHANOV, R.A., KUZMICHEV, S.D., USMANOV, R.A. & VORONA, N.A. 2018 Investigation of the influence of injection parameters on particles motion in electric and magnetic fields for designing plasma separation technique. *Plasma Phys. Rep*. **44** (12), 1104–1113.

SMIRNOV, V.S., EGOROV, R.O., KISLENKO, S.A., ANTONOV, N.N., SMIRNOV, V.P. & GAVRIKOV, A.V. 2020 Simulation of ion flux of actinides and uranium fission products in the plasma separator with a potential well. *Phys. Plasmas* **27** (11), 113503.

SOLDATKINA, E.I., BAGRYANSKY, P.A. & SOLOMAKHIN, A.L. 2008 Influence of the radial profile of the electric potential on the confinement of a high-β two-component plasma in a gas-dynamic trap. *Plasma Phys. Rep*. **34** (4), 259–264.

SONG, P., GOMBOSI, T.I. & RIDLEY, A.J. 2001 Three-fluid Ohm's law. *J. Geophys. Res.: Space Phys*. **106** (A5), 8149–8156.

VORONA, N.A., GAVRIKOV, A.V., KUZMICHEV, S.D., LIZIAKIN, G.D., MELNIKOV, A.D., MURZAEV, Y.A., SMIRNOV, V.P., TIMIRKHANOV, R.A. & USMANOV, R.A. 2019 Large Helicon plasma source for the method of plasma separation of spent nuclear fuel and radioactive waste. *IEEE Trans. Plasma Sci*. **47** (2).

ZOLOTUKHIN, D.B., DANIELS, K.P., BRIEDA, L. & KEIDAR, M. 2020 Onset of the magnetized arc and its effect on the momentum of a low-power two-stage pulsed magneto-plasma-dynamic thruster. *Phys. Rev.* E **102** (2), 021203(R).

ZWEBEN, S.J., GUEROULT, R. & FISCH, N.J. 2018 Plasma mass separation. *Phys. Plasmas* **25** (9), 90901.

https://doi.org/10.1017/S0022377821000829 Published online by Cambridge University Press